

Kyu Yoon<sup>1,2</sup>   
 Hyun Wook Jung<sup>1\*</sup>   
 Myung-Suk Chun<sup>2,3</sup>

<sup>1</sup>Department of Chemical and Biological Engineering, Korea University, Seongbuk-gu, Seoul, Republic of Korea

<sup>2</sup>National Agenda Research Division, Korea Institute of Science and Technology (KIST), Seoul, Republic of Korea

<sup>3</sup>Bio-Medical Department, KIST School, Korea University of Science and Technology, Seoul, Republic of Korea

Received October 10, 2019  
 Revised February 21, 2020  
 Accepted February 21, 2020

## Research Article

# Two-phase flow in microfluidic-chip design of hydrodynamic filtration for cell particle sorting

As one of the flow-based passive sorting, the hydrodynamic filtration using a microfluidic-chip has shown to effectively separate into different sizes of subpopulations from cell or particle suspensions. Its model framework involving two-phase Newtonian or generalized Newtonian fluid (GNF) was developed, by performing the complete analysis of laminar flow and complicated networks of main and multiple branch channels. To predict rigorously what occurs in flow fields, we estimated pressure drop, velocity profile, and the ratio of the flow fraction at each branch point, in which the analytical model was validated with numerical flow simulations. As a model fluid of the GNF, polysaccharide solution based on Carreau type was examined. The objective parameters aiming practical channel design include the number of the branches and the length of narrow section of each branch for arbitrary conditions. The flow fraction and the number of branches are distinctly affected by the viscosity ratio between feed and side flows. As the side flow becomes more viscous, the flow fraction increases but the number of branches decreases, which enables a compact chip designed with fewer branches being operated under the same throughput. Hence, our rational design analysis indicates the significance of constitutive properties of each stream.

### Keywords:

Cell sorting / Channel design / Hydrodynamic filtration / Microfluidic-chip / Two-phase flow  
 DOI 10.1002/elps.201900394

## 1 Introduction

The separation and sorting of suspended cells or particles have long been important in various industrial processing, biomedical applications, and preparatory analysis system. Traditional methods are proven to have high efficiency and reproducibility, but they remain limited by needs for a large sample volume, batch mode, and multistep preparation. It is noteworthy that fluid physics-based continuous cell particle separations at the micrometer scale have been widely implemented due to their very low sample volume, faster treatments, etc. [1–5]. Microfluidic systems have been recognized as a practical tool for efficient sorting with the benefit of microfabrication, and several types of microfluidic cell sorters are commercially available [6–10]. Instead of employing external force fields in the active sorting [11, 12], the passive sorting relies on the inherent microfluidic features underlying the flow field, channel geometry, and particle interactions. The passive sorting [13–23] has the advantage

not to use external fields, but their efficiency is usually lower than that in the active sorting. Thus, passive sorting devices require possible design variants aiming improved performance with properly designed microfluidic-chip and complementary solution input.

As one of the passive sorting techniques, the hydrodynamic filtration (HDF) has shown to effectively separate various sizes of living cell particles by using a microfluidic chip with multiple branch channels [15–18]. The role of these branches, which is similar to the pores in conventional crossflow filtration, lies in removing carrier fluid and particle focusing. In Fig. 1A, bidisperse suspended cells are continuously introduced into the main channel and the selective extraction of streamlines caused by side flow is controlled by the flow fraction at each branch for separation. Only the stream near the sidewall enters the branches, with the amount of fluid leaving the main channel being determined by the flow distribution related to the hydraulic flow resistances [24]. To achieve the efficient focusing, a deep channel with larger height  $H$  than width  $W$  ( $H \geq 4W$ ) is considered here and all branches slanted to the main channel with  $60^\circ$  are in parallel to the direction of the side channel. Design variants in terms of flow field, flow fraction, and channel networks eventually

**Correspondence:** Dr. Myung-Suk Chun, National Agenda Research Division, Korea Institute of Science and Technology (KIST), Seoul 02792, Republic of Korea  
 E-mail: mschun@kist.re.kr

**Abbreviations:** BC, Bird–Carreau; GNF, generalized Newtonian fluid; HDF, hydrodynamic filtration

\*Additional Corresponding Author: Professor Hyun Wook Jung  
 E-mail: hwjung@grtrkr.korea.ac.kr

**Color Online:** See the article online to view Figs. 1, 2, 4, and 5 in color.

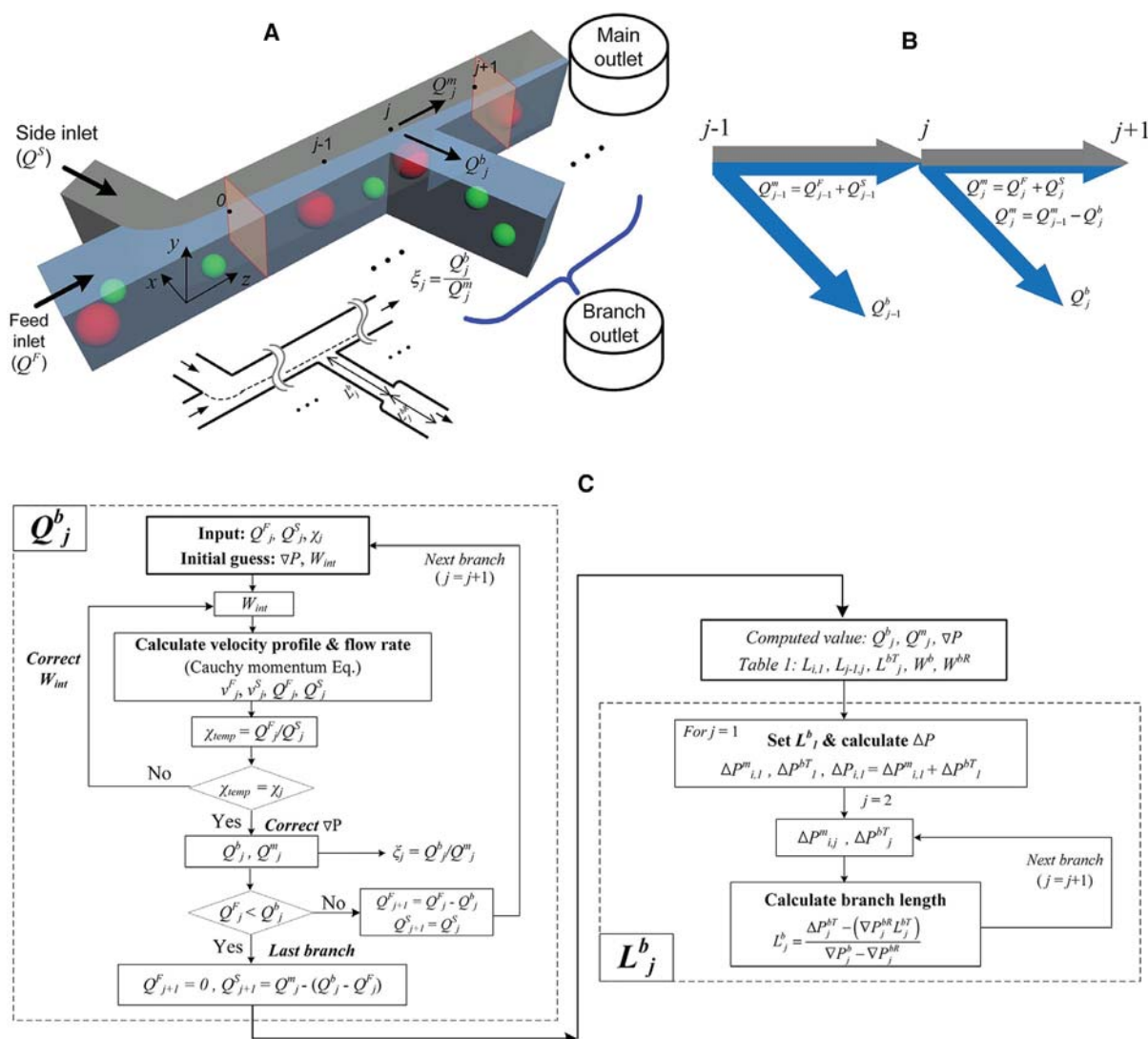


**Figure 1.** Schematics of (A) HDF microfluidic-chip for bimodal sorting with two-phase flow fraction, where a small cell particle flows into the branch channel, whereas a large cell particle passes along the main channel. (B) The inlet flow consisting of  $Q^F$  and  $Q^S$  and flow fraction between  $Q^b$  and  $Q^m$  at branch point, where feed and side streams are represented by blue and gray colors, respectively. (C) The framework of the numerical algorithm employed in this study.

determine the sorting efficiency with respect to the recovery of different outlets and the purity of each target particle.

Note that cell suspensions represented as the complex fluid are usually more viscous than the simple fluid of suspension medium (e.g., PBS) supplied into the side channel. In some cases, viscosity thickeners, such as those of polysaccharides, can be added in the side flow to attempt possible higher focusing. Moreover, many biological fluids (e.g., protein and DNA solutions, blood, etc.) exhibit non-Newtonian characteristics [25, 26]. Therefore, for a practical portrayal of the flow stream, it is more appropriate to regard the Newtonian and generalized Newtonian fluid (GNF) as a two-phase model comprising feed and side flows with different viscosities. In this study, we examine the effects of two-phase flow on the rational design of HDF chip for label-free cell sorting, which has not been reported yet. Based on the analyti-

cal model in microfluidic networks with multiple branches, both the number of branch channels and the length of narrow section of each branch are estimated. Illustrative computations are performed providing viscosity ratio ranging 0.1~20, which can be favorably accessible real sorting.

## 2 Computational Methods

### 2.1 Model development

For the GNF at a steady-state laminar flow, the velocity field driven by pressure gradient is given by Cauchy momentum equation, such that

$$\nabla \cdot \tau = \nabla P. \tag{1}$$

Here, the viscous stress tensor  $\boldsymbol{\tau}$  can be related to the rate of deformation tensor  $\boldsymbol{D}$  as  $\boldsymbol{\tau} = 2\eta(\gamma)\boldsymbol{D}$ , where  $\eta$  is the viscosity,  $\gamma$  is the shear rate, and  $\boldsymbol{D} \equiv (\nabla\boldsymbol{v} + \nabla\boldsymbol{v}^T)/2$  with the velocity vector  $\boldsymbol{v}$  [27]. The shear rate can be defined in terms of the second invariant of  $2\boldsymbol{D}$  as

$$\gamma = (2\boldsymbol{D} : \boldsymbol{D})^{1/2} = \left[ 2 \sum_p \sum_q D_{pq} D_{qp} \right]^{1/2}. \quad (2)$$

One should note that the trace of  $\boldsymbol{D}$  is also zero from the continuity relation and the transpose of deformation tensor is equal. Then, the shear rate in the Cartesian coordinates in Fig. 1A yields

$$\begin{aligned} \gamma &= \sqrt{2} \left[ -2D_{11}D_{22} - 2D_{22}D_{33} - 2D_{33}D_{11} \right. \\ &\quad \left. + 2(D_{12}^2 + D_{13}^2 + D_{23}^2) \right]^{1/2} \\ &= \left[ \left( \frac{\partial v_x}{\partial y} + \frac{\partial v_y}{\partial x} \right)^2 + \left( \frac{\partial v_y}{\partial z} + \frac{\partial v_z}{\partial y} \right)^2 + \left( \frac{\partial v_z}{\partial x} + \frac{\partial v_x}{\partial z} \right)^2 \right. \\ &\quad \left. - \left( \frac{\partial v_x}{\partial x} \frac{\partial v_y}{\partial y} \right) - \left( \frac{\partial v_y}{\partial y} \frac{\partial v_z}{\partial z} \right) - \left( \frac{\partial v_z}{\partial z} \frac{\partial v_x}{\partial x} \right) \right]^{1/2}, \quad (3) \end{aligned}$$

and the concerned components of  $\boldsymbol{\tau}$  can be  $\tau_{zx} = \eta\gamma_{zx}$ . For a Newtonian fluid with constant viscosity, Eq. (1) becomes  $\eta\nabla^2\boldsymbol{v} = \nabla P$ .

As presented in Fig. 1A, the cell suspension is introduced into the feed inlet with flow rate  $Q^F$  and the buffer solution is supplied into the side inlet with  $Q^S$ , where its total inlet flow is  $Q^F + Q^S$ . The flow at a reference point ( $j = 0$ ) starts to form fully-developed velocity profile, since the distance from a junction of main and side channels to the first branch point is designed to be larger than the entrance length [28]. Since the particle Reynolds number is really in the order of less than unity, the inertial lift force of suspended particle from channel wall is negligible [29, 30]. Convection happens much faster than diffusion owing to the high Péclet number so that mixing of feed and side streams is quite slow [31]. For the interface boundary  $W_{\text{int}}$  between two adjacent immiscible streams,  $Q_j^F$  and  $Q_j^S$  in the forefront of the branch point  $j$  can be obtained by integrating velocity profile of rectangular-slit geometry,

$$Q_j^F = \int_0^H \int_0^{W_{\text{int}}} v_z^F(x) dx dy, \quad (4)$$

$$Q_j^S = \int_0^H \int_{W_{\text{int}}}^W v_z^S(x) dx dy. \quad (5)$$

Then, we define the inlet flow ratio  $\chi_j$  as the flow ratio of  $Q_j^F$  to  $Q_j^S$ ,

$$\chi_j \equiv Q_j^F / Q_j^S. \quad (6)$$

Either Newtonian fluid or GNF is applied to Eq. (1) and both stress and velocity of feed flow at the interface between feed and side streams are matched with those of side flow, as  $\boldsymbol{\tau}^F(W_{\text{int}}) = \boldsymbol{\tau}^S(W_{\text{int}})$ ;  $v^F(W_{\text{int}}) = v^S(W_{\text{int}})$  [32]. No-slip boundary condition is applied at  $x = 0$  and  $W$ , as  $v^F(0) = 0$ ;  $v^S(W) = 0$ . In Eqs. (4) and (5),  $v_z(x)$  for Newtonian fluids has analytical form

for different viscosity of  $\eta^F$  and  $\eta^S$ . From the simultaneous solution according to the matching condition, one can obtain the axial velocity of each flow, respectively

$$v_z^F(x) = -\frac{1}{2\eta^F} \frac{\partial P}{\partial z} x^2 + c_1 x \quad \text{for } 0 \leq x \leq W_{\text{int}}, \quad (7)$$

$$v_z^S(x) = -\frac{1}{2\eta^S} \frac{\partial P}{\partial z} x^2 + c_2 x + c_3 \quad \text{for } W_{\text{int}} \leq x \leq W \quad (8)$$

where

$$c_1 = \left[ \left( \frac{1}{\eta^F} - \frac{1}{\eta^S} \right) \frac{\partial P}{\partial z} W_{\text{int}}^2 + \frac{1}{2\eta^S} \frac{\partial P}{\partial z} W^2 \right] / \left[ \left( 1 - \frac{\eta^F}{\eta^S} \right) W_{\text{int}} + \frac{\eta^F}{\eta^S} W \right], \quad (9)$$

$$c_2 = \frac{\eta^F}{\eta^S} c_1, \quad (10)$$

$$c_3 = -c_2 W + \frac{1}{2\eta^S} \frac{\partial P}{\partial z} W^2. \quad (11)$$

The spanwise average velocity of rectangular-slit geometry is obtained by integrating the corresponding Eqs. (7) and (8) along the  $x$ -direction, and further integrating over the height along the  $y$ -direction becomes  $Q_j^F$  and  $Q_j^S$  at the forefront of the branch point  $j$  in the main channel, as follows

$$Q^F = \int_0^H \int_0^{W_{\text{int}}} v_z^F(x) dx dy = -\frac{H}{6\eta^F} \frac{\partial P}{\partial z} W_{\text{int}}^3 + \frac{c_1 H}{2} W_{\text{int}}^2 \quad (12)$$

$$\begin{aligned} Q^S &= \int_0^H \int_{W_{\text{int}}}^W v_z^S(x) dx dy = -\frac{H}{6\eta^S} \frac{\partial P}{\partial z} (W^3 - W_{\text{int}}^3) \\ &\quad + \frac{c_2 H}{2} (W - W_{\text{int}}) + c_3 H (W - W_{\text{int}}). \quad (13) \end{aligned}$$

Note that  $v_z(x)$  for GNFs should be numerically solved because each viscosity depends on the shear rate.

In Fig. 1A, sorted small particles through the multiple branches are collected into the branch outlet, and remained large particles in the main channel are collected into the main outlet. Branch channels are equally spaced and have the same width  $W^b$  that is smaller than main channel width  $W$ , and  $H$  is uniform over the entire channel network. We set the cut-off width  $W_C$ , representing the virtual boundary of fluid layer that will divide total inlet streams into two parts. The target spherical particles with a hydrodynamic center less than a  $W_C$  are expected to be sorting out. As shown in Fig. 1B, the flow fraction at each branch should be estimated by defining the ratio of flow fraction  $\xi$  as the ratio of the flow rate between branch stream and main stream at a specific  $j$ th branch point

$$\xi_j \equiv Q_j^b / Q_j^m. \quad (14)$$

Here,  $Q_j^b$  indicates the flow rate entering the  $j$ th branch channel computed by  $Q_j^b = \int_0^H \int_0^{W_C} v_z^m(x) dx dy$ .  $Q_j^m$  represents the flow rate between branch points  $j$  and  $j+1$  in main channel, allowing  $Q_j^m = Q_{j-1}^m - Q_j^b$ .

## 2.2 Computation scheme for HDF chip design with channel network

Branches connected to relevant outlet are composed of multiple channels for effective separation of particles. Branches are designed to have narrow and wide segments that make the total lengths of each channel uniform (cf., 3 cm in this study) by adjusting their hydraulic flow resistances. The narrow segment exists for actual application of pressure drop, and the wide segment works as a kind of reservoir with a relatively larger width in order to prevent the unwanted reverse flow during particle discharge. Table 1 summarizes the design parameters we have used in this study. The aspect ratio of the channel cross-section (i.e.,  $H/W$ ) must be higher than at least 8 to get a perfect slit channel. However, such a deep channel (or complementary shallow channel) is rarely used in practical microfluidic-chips owing to the difficulty of fabrications. The condition of  $H/W = 4$  (named as rectangular-slit geometry) is applied in our computations, which can be useful to experimental scientists. The interface boundary  $W_{\text{int}}$  between two adjacent immiscible streams is actually the key parameter to determine the number of branches and the lengths of each branch. In the case of  $H/W = 4$ , its deviation of one-dimensional solution for the slit from the rectangular-slit is evaluated very low (cf., relative difference of 2.95%), along with the low deviation in the total flow rate. The multiple unknown variables as target parameters in our chip design are the number of branch channels, the length of narrow section of each branch channel, and the length between the last branch and main outlet.

**Table 1.** Design parameters and their values

Condition	Dimension	Notation	Values	
Flow ratio	Inlet flow	$Q^F/Q^S$	1/3	
Flow rate	Feed	$Q_j^F$	to be computed	
	Side	$Q_j^S$	to be computed	
	Branch	$Q_j^b$	to be computed	
	Main	$Q_j^m$	to be computed	
Main channel	Height	$H$	200 $\mu\text{m}$	
	Width	$W$	50 $\mu\text{m}$	
	Length	Inlet	$L_{i,1}^m$	500 $\mu\text{m}$
		Inter-branch point	$L_{j-1,j}^m$	3 mm
		Outlet	$L_O^m$	to be computed
	Interface boundary	$W_{\text{int}}$	to be computed	
	Cut-off width	$W_C$	12.5 $\mu\text{m}$	
Branch channel	Height	$H$	200 $\mu\text{m}$	
	Width	Narrow section	$W_j^b$	45 $\mu\text{m}$
		Wide section	$W_j^{\text{bR}}$	100 $\mu\text{m}$
	Number	$N^b$	to be computed	
	Length	Total	$L_j^{\text{bT}}$	30 mm
		Narrow section	$L_j^b$	to be computed
		Wide section	$L_j^{\text{bR}}$	to be computed

### 2.2.1 $Q^b$ and $N^b$ computations

In essence, the number of branches and each flow rate  $Q_j^b$  for sorting can be iteratively determined by resolving  $v_z(x)$ ,  $\nabla P$ , and  $\chi_j$  at each branch point with initial guess of  $W_{\text{int}}$ , as illustrated in Fig. 1C. From the inlet flow condition, the velocity profile is first determined for the initial guess of  $\nabla P$  and  $W_{\text{int}}$ , and then  $Q_j^F$  and  $Q_j^S$  are calculated from Eqs. (9)–(13).  $W_{\text{int}}$  is estimated by comparing the values between calculated  $\chi_j$  from Eq. (6) and  $\chi_j$  for the inlet condition. This  $\chi_j$  criterion allows us to quantify the correct  $\nabla P$ . Next procedure is to compute  $Q_j^b$ ,  $Q_j^m$ , and correspondent flow fraction ratio by integrating velocity profile with respect to  $W_C$ .

The criterion specified with a magnitude between  $Q_j^F$  and  $Q_j^b$  allows to determine the number of branch channels (cf., Fig. 1B). If  $Q_j^F > Q_j^b$ , iterations are performed to compute for next branch as  $Q_{j+1}^F = Q_j^F - Q_j^b$  and  $Q_{j+1}^S = Q_j^S$ , for which  $Q_{j+1}^F$ ,  $Q_{j+1}^S$ , and correspondent  $\chi_{j+1}$  become input condition at  $(j+1)$ th branch. If  $Q_j^F < Q_j^b$ , it needs the  $(j+1)$ th branch as the last branch because cell particles in the feed flow are completely separated therein, remaining flows of  $Q_{j+1}^F = 0$  and  $Q_{j+1}^S = Q_j^S - (Q_j^b - Q_j^F)$  in the main channel are collected into the main outlet. Thus, the appropriate number of branches is determined from controlling flow rate distribution until inlet flow ratio goes to zero.

### 2.2.2 $L^b_j$ and $L^{\text{bR}}_j$ computations

Next, the lengths of narrow sections of individual branch can be sequentially obtained from the relationship of equality for pressure drop regarding each branch channel. In the channel networks, the flow rate is described by the hydraulic flow resistance  $R$  such that

$$Q \equiv \frac{\Delta P}{R} \quad (15)$$

where  $R$  is expressed as a function of  $\eta(Q)$ ,  $L$ ,  $W$ ,  $H$ , and  $\chi$ . The pressure drop at the main channel between inlet and branch point  $j$  can be given as

$$\Delta P_{i,j}^m = \Delta P_{i,j-1}^m + \Delta P_{j-1,j}^m. \quad (16)$$

Since  $\Delta P_{j-1,j}^m = R_{j-1,j}^m Q_{j-1,j}^m$  and  $Q_{j-1,j}^m$  is represented by subtracting output flows at branches from 1st to  $(j-1)$ th from the total inlet flow  $Q^F + Q^S$ , the pressure drop at the corresponding interval is estimated as

$$\Delta P_{j-1,j}^m = R_{j-1,j}^m \left( (Q^F + Q^S) - \sum_1^{j-1} Q_j^b \right). \quad (17)$$

Total pressure drop at each branch channel can be expressed as the pressure drops in narrow section as well as wide section

$$\Delta P_j^{\text{bT}} = \nabla P_j^b L_j^b + \nabla P_j^{\text{bR}} (L_j^{\text{bT}} - L_j^b) \quad (18)$$

where  $\nabla P$  is the pressure gradient (i.e., pressure drop per unit length) and  $L^{bT_j} - L^b$  corresponds to the length of wide section  $L^{bR_j}$ . The pressure drops between inlet and each outlet point are set to be the same from that the main and all branch channels are open to the atmosphere,  $\Delta P_{i,1} = \dots = \Delta P_{i,j} = \dots = \Delta P_{i,O}$ , then pressure drops at each branch are sequentially resolved. The pressure drop at the first branch can be obtained for the initial guess of its narrow section length  $L^b_1$ , followed by computing the overall pressure drop with  $\Delta P_{i,j} = \Delta P^m_{i,j} + \Delta P^{bT}_j$ .

Our final objective parameter  $L^b_j$ , derived from Eq. (18), can be obtained from

$$L^b_j = \frac{\Delta P^{bT}_j - (\nabla P^{bR}_j L^{bT}_j)}{\nabla P^b_j - \nabla P^{bR}_j} \quad (19)$$

where the repeat step of computation is performed by another iteration scheme on the above condition  $\Delta P_{i,1} = \Delta P_{i,j}$  in the multiple branches. The iterative computations were done for all branch points. Our model framework was solved with implementation of the Matlab (Mathworks, MA).

### 3 Results and discussion

Figure 2 shows two immiscible Newtonian fluids of feed and side streams are flowing in the  $z$ -direction with a liquid-liquid flat interface, and this interface moves toward the sidewall adjacent to the branches. The bimodal distribution of cells particles is considered to be separated with small particles less than  $25 \mu\text{m}$  diameter and large ones ranging  $25$  to  $50 \mu\text{m}$  diameter. The cut-off width  $W_C$  is given as a half of target particles (i.e.,  $12.5 \mu\text{m}$ ), expecting that the small particles would be removed through the branch channels.

In Fig. 3, the viscosity ratio  $\eta^F/\eta^S$  is changed based on the deionized (DI) water ( $\eta = 0.001 \text{ Pa}\cdot\text{s}$ ), which is a simple fluid and commonly used as a background medium for cell suspensions, biological fluids, and PBS. The value of  $\eta^F/\eta^S = 1$  means that DI water is introduced into the feed as well as side inlets. It should be emphasized that the interface position ( $x = W_{int}$ ) decreases with decreasing  $\chi_j$ , indicating the higher focusing on the sidewall of the main channel for higher side flow or higher  $\eta^S$ . According to the small particle Reynolds number in this study, the viscous drag force mainly acts on the suspended particles, which is related to the drag coefficient [33]. As  $\eta^S$  increases, the steep change occurs in shear rate profiles, which may affect the distribution of cell particles associated to local disturbances in the surrounding two-phase flow fields, but particle transport would follow the streamlines owing to the low fluid inertia. As being reliable behavior, all streamlines located inside of  $W_C$  enter the branch channel. Small and large particles allows that suspended particles are separated according to their positions of center-of-mass with respect to  $W_C$ .

In Fig. 4, the flow fraction ratio in the Newtonian fluid decreases with increasing viscosity ratio  $\eta^F/\eta^S$ , but it does not depend on the total inlet flow. In order to figure out notable

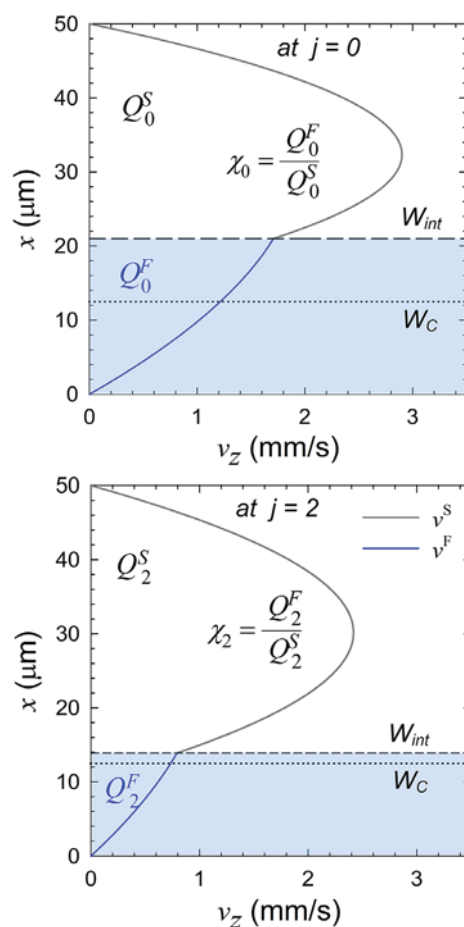


**Figure 2.** The exemplar axial velocity profile in a two-phase flow with different viscosities at the reference and the 2nd branch points, where total inlet flow is  $1 \mu\text{L}/\text{min}$  with  $\chi_i = 1/3$  and  $\eta^F/\eta^S = 5$ .

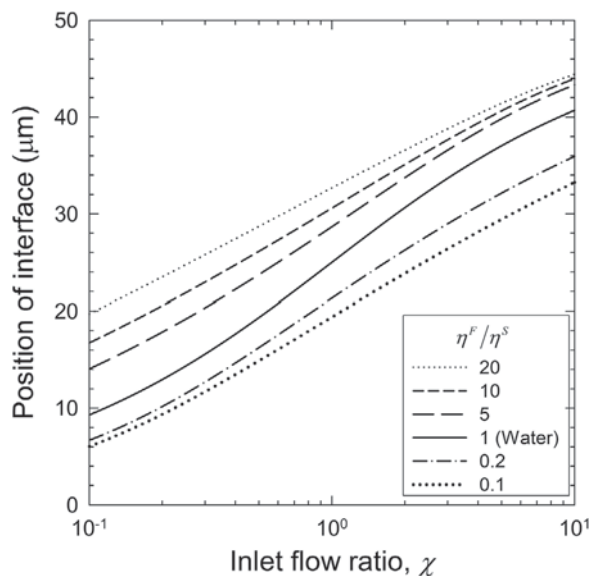


**Figure 3.** The position of interface with variations of inlet flow ratio between feed and side flows for different viscosity ratios  $\eta^F/\eta^S$ .

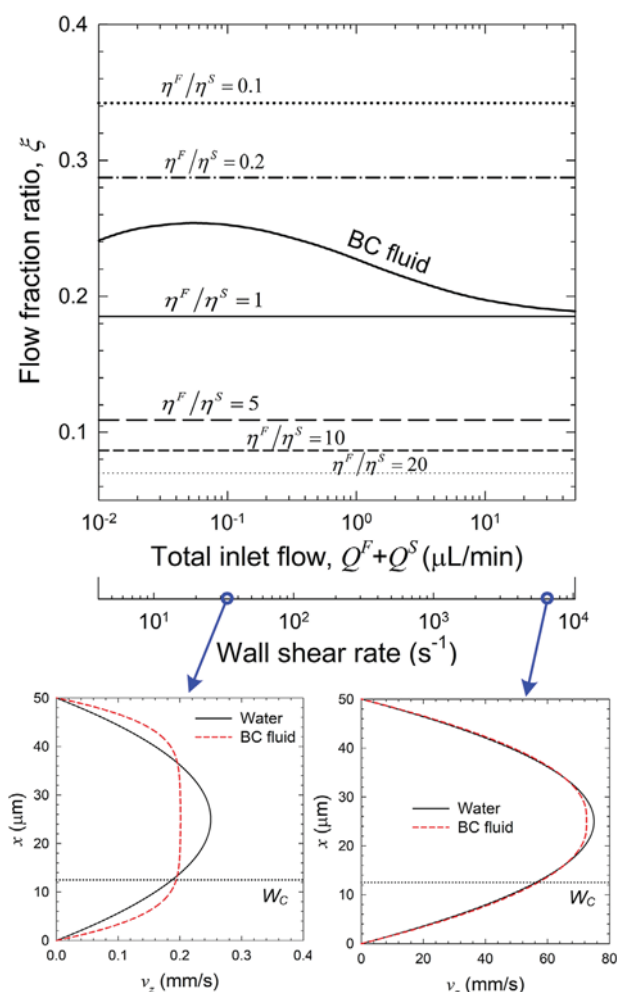


**Figure 4.** The flow fraction with variations of total inlet flows for different  $\eta^F/\eta^S$ , where the insets show comparative velocity profiles between DI water and BC fluid obtained at  $Q^m = 0.1$  and  $30 \mu\text{L}/\text{min}$ . Parameters of BC fluid are  $\eta_0 = 0.79 \text{ Pa}\cdot\text{s}$ ,  $\eta_\infty = 2.5 \text{ mPa}\cdot\text{s}$ ,  $n = 0.2$ , and  $\lambda = 3 \text{ s}$  for  $0.2 \text{ wt}\%$  schizophyllan solution.

feature of the GNF, we adopt the Bird–Carreau (BC) model, which is referred to as a modified version of the Carreau–Yasuda model for inelastic fluids [26, 27]. Its viscosity describes typical biological fluids as a function of the velocity field:  $\eta = \eta_\infty + (\eta_0 - \eta_\infty)[1 + (\lambda\gamma)^2]^{(n-1)/2}$ , with the zero-shear viscosity  $\eta_0$ , infinite-shear viscosity  $\eta_\infty$ , power-law index  $n$ , and relaxation time constant  $\lambda$  corresponding to  $1/\gamma$  at which the fluid changes from Newtonian to shear-thinning (pseudoplastic) behavior. We provide a dilute solution of polysaccharide schizophyllan as a model fluid, and the values of parameters determined from rheological measurements are provided in the figure caption. When the BC fluid flows in the main channel, the same BC fluid is supplied into both feed and side channels to clarify what the different contribution is in the GNF as compared to the Newtonian fluid. The flow fraction ratio of the BC fluid exceeds that of the DI water, meaning higher flowing into branch channels. Of interest here is that, with increasing flow rate, the flow fraction

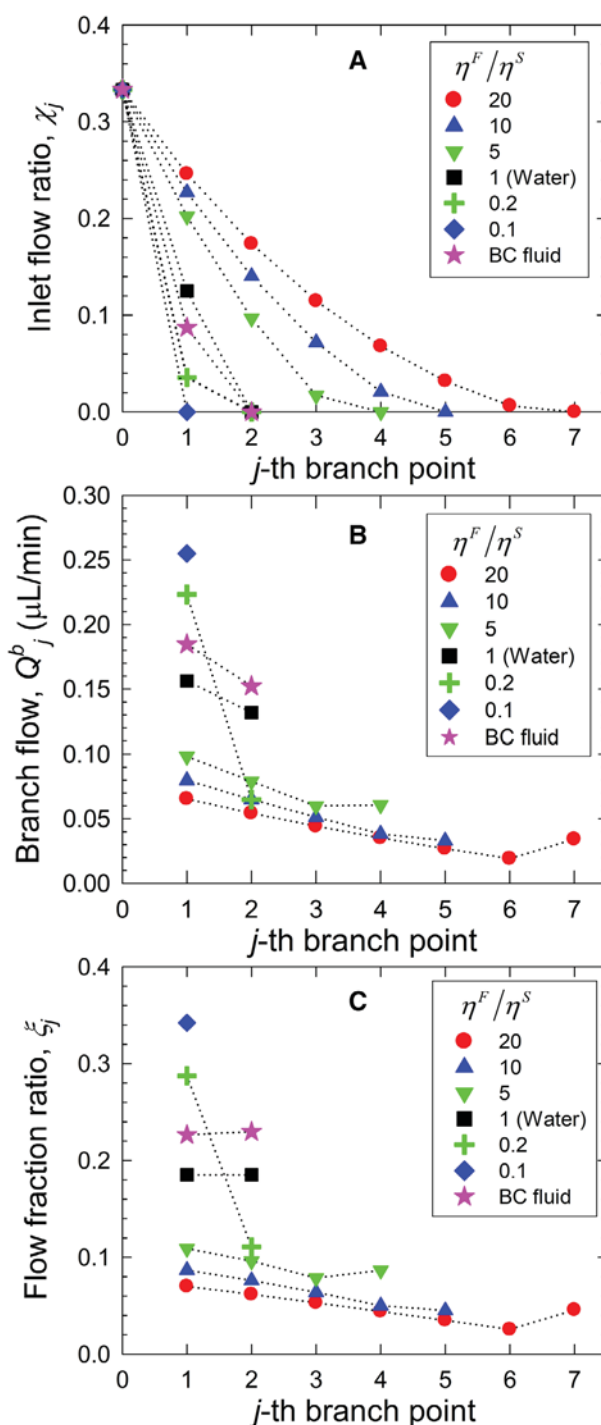


**Figure 5.** The variations of (A) inlet flow ratio, (B) flow rate of individual branch channels, and (C) the ratio of the flow fraction at each branch point with variations of viscosity ratios.

rises to a maximum value and then falls to get the DI water case. As provided in insets, the axial velocity of BC fluid at low flow rate tends to be horizontal along the spanwise axis by spreading to both sides of the wall, in contrast to the Newtonian fluid. Accordingly, as the spreading portion becomes

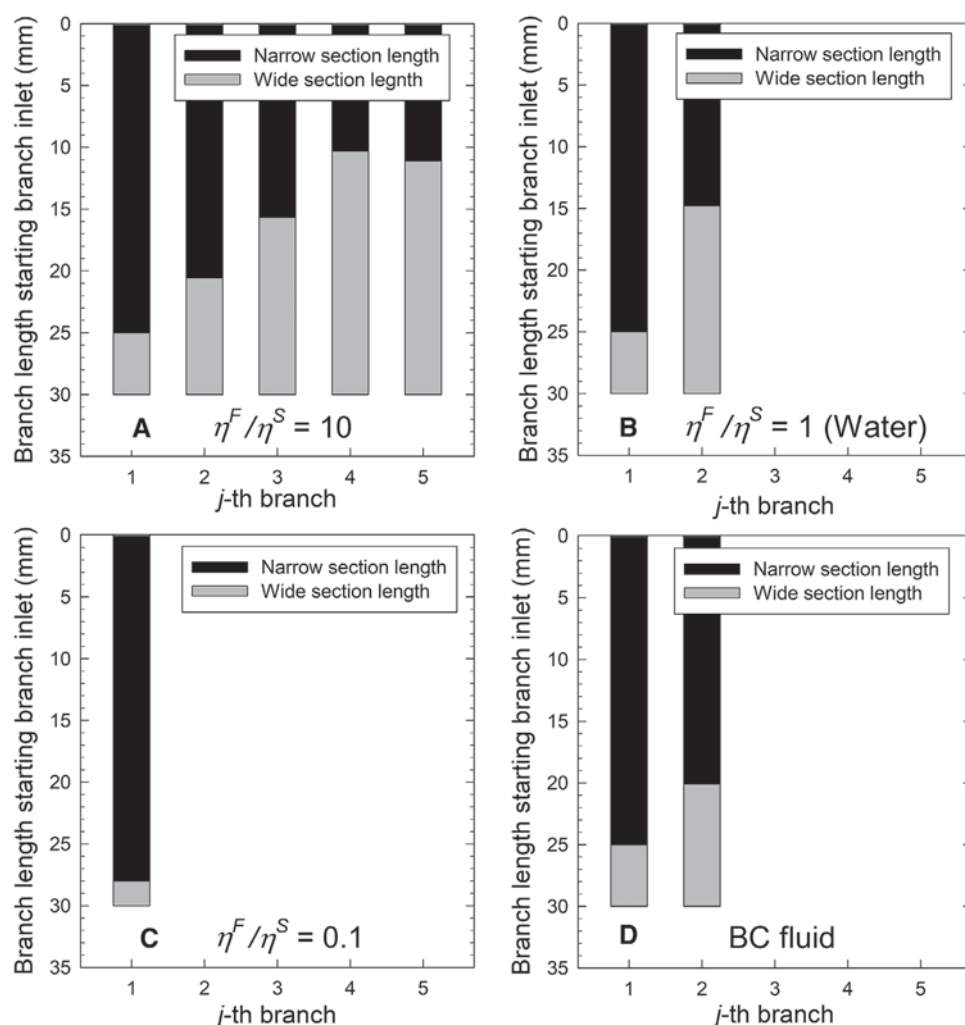


**Figure 6.** The variations of channel design of multiple branches for (A)  $\eta^F/\eta^S = 10$ , (B)  $\eta^F/\eta^S = 1$  (i.e., DI water), (C)  $\eta^F/\eta^S = 0.1$ , and (D) BC fluid. Here, branches consist of narrow and wide segments that make their total lengths uniform as 3 cm.

larger near the sidewall, entering branches can be enhanced in GNFs.

The number of branches can be determined by the criterion that branch channels should be designed until  $W_{\text{int}}$  becomes less than  $W_C$ , in which small and large particles are completely separated. Figure 5 shows that the number of branches clearly decreases with decreasing  $\eta^F/\eta^S$  due to higher focusing effect, as displayed in Fig. 3. As the branch point moves toward the end of the main channel,  $\chi_j$  is reduced to zero at the last branch from 1/3. Notable behavior of two-phase Newtonian fluids or GNFs compared to the single-phase Newtonian one should be a variation of the flow fraction along the branch point, caused by the variable velocity profile of two-phase flow according to a change of interface position. It results in the increases of flow rate as well as corresponding  $\xi_j$  at the last branch for  $\eta^F/\eta^S > 1$ .

The flow simulation was performed using COMSOL Multiphysics 5.3a [34] to compare with the results obtained from our model. This numerical approach for the momentum equation incorporated with the phase-field method is applied to solve entire flow fields and underlying boundary

conditions at the interface between immiscible feed and side flows. The flow fields for overall channel networks are estimated regarding Newtonian and BC fluids, according to the prescribed condition of each flow rate. From the estimated flow fields, coupling between the particle and the fluid can account for a trajectory of single particle, in conjunction with the time evolution of particle transport. Further studies are required to access the detailed analysis of the particle tracing.

Figure 6 shows the design of branch channel network for different viscosity conditions, where each branch is designed to consist of narrow and wide sections and the narrow section acts to actually control the pressure drop [17]. The number of branches becomes obviously different, despite of the same throughput processing. Employing a higher viscous side flow than the feed flow can fulfill sorting by a chip simply designed with fewer branches. Newtonian fluids show the length of each narrow section is monotonically shortened from the longest first branch, as the branch moves toward the last one. The last branch length for  $\eta^F/\eta^S > 1$  slightly increases owing to the reduced flow resistance therein caused by the entrance of low viscous side flow, as explained in Fig. 5.

Our framework is useful to provide comparative information, serving as an important bridge between modeling and experiments, which is necessary for the highly efficient sorting.

## Nomenclature

$D$	Rate of deformation tensor [1/s]
$H$	Channel height [ $\mu\text{m}$ ]
$L_{i,1}^m$	Length between main inlet and first branch channel [ $\mu\text{m}$ ]
$L_j^b$	Narrow-section length of $j$ th branch [ $\mu\text{m}$ ]
$L_j^{bR}$	Wide-section length of $j$ th branch [ $\mu\text{m}$ ]
$L_j^{bT}$	Total length of $j$ th branch [ $\mu\text{m}$ ]
$L_0^m$	Length between last branch channel and main outlet [ $\mu\text{m}$ ]
$n$	Power-law index [-]
$P$	Pressure [Pa]
$\Delta P_j^b$	Pressure difference at narrow section of $j$ th branch [Pa]
$\Delta P_j^{bR}$	Pressure difference at wide section of $j$ th branch [Pa]
$\Delta P_j^{bT}$	Total pressure difference at $j$ th branch [Pa]
$\Delta P_{ij}^m$	Pressure difference at main channel between inlet and $j$ th branch point [Pa]
$\Delta P_{ij}$	Overall pressure difference between inlet and $j$ th branch outlet [Pa]
$Q$	Flow rate [ $\mu\text{L}/\text{min}$ ]
$Q_j^b$	Flow rate at $j$ th branch channel [ $\mu\text{L}/\text{min}$ ]
$Q_j^F$	Flow rate of feed stream at $j$ th branch point [ $\mu\text{L}/\text{min}$ ]
$Q_j^m$	Flow rate of main stream at $j$ th branch point [ $\mu\text{L}/\text{min}$ ]
$Q_j^S$	Flow rate of side stream at $j$ th branch point [ $\mu\text{L}/\text{min}$ ]
$R$	Hydraulic resistance in channel [ $\text{N}\cdot\text{s}/\text{m}^3$ ]
$v_z$	Axial fluid velocity [mm/s]
$W$	Main channel width [ $\mu\text{m}$ ]
$W_j^b$	Narrow-section width of $j$ th branch [ $\mu\text{m}$ ]
$W_j^{bR}$	Wide-section width of $j$ th branch [ $\mu\text{m}$ ]
$W_C$	Cut-off width [ $\mu\text{m}$ ]
$W_{\text{int}}$	Interface boundary [ $\mu\text{m}$ ]
<b>Greek letters</b>	
$\gamma$	Shear rate [1/s]
$\eta$	Fluid viscosity [Pa·s]
$\eta_0$	Zero-shear viscosity [Pa·s]
$\eta_\infty$	Infinite-shear viscosity [Pa·s]
$\lambda$	Relaxation time constant [s]
$\xi_j$	Ratio of the flow fraction between branch and main flows at $j$ th branch point [-]
$\tau$	Cauchy stress tensor [Pa]
$\chi_j$	Ratio of the flow rate between feed and side stream at $j$ th branch point [-]
<b>Subscripts</b>	
$i$	Main inlet
int	Interface
$j$	Branch point
$O$	Main outlet
<b>Superscripts</b>	
$b$	Branch channel
bR	Wide section of branch channel
bT	Total branch channel
$F$	Feed
$m$	Main channel
$S$	Side

## 4 Concluding remarks

In summary, several cases of two-phase Newtonian fluids with different viscosity ratios and the BC fluid as a typical GNF were investigated, for the cell sorting with various types of suspension medium. Our model can be validated by the fact that analytical results are shown to be in good agreement with the numerical flow simulations. Our results from the present model framework for HDF would be an emphasis on the enhanced particle focusing due to the increase of the flow fraction with decreasing inlet flow ratio ( $Q_j^F/Q_j^S$ ) and viscosity ratio ( $\eta^F/\eta^S$ ), leading to a compact chip designed with fewer branches. As a final remark, both the two-phase flow and the GNF get nontrivial implications in the conceptual design and physical prototype of HDF chip capable of enhanced sorting efficiency.

*This work was supported by the Korea Institute of Science and Technology (project no. 2E30580) provided to M.-S. Chun and by the National Research Foundation (NRF) of Korea grant (nos. 2016R1A5A1009592 and 2017R1E1A1A01075107) provided to H.W. Jung.*

*The authors have declared no conflict of interest.*

## 5 References

- [1] Knight, J. B., Vishwanath, A., Brody, J. P., Austin, R. H., *Phys. Rev. Lett.* 1998, *80*, 3863–3866.
- [2] Stone, H. A., Stroock, A. D., Ajdari, A., *Annu. Rev. Fluid Mech.* 2004, *36*, 381–411.
- [3] Lenshof, A., Laurell, T., *Chem. Soc. Rev.* 2010, *39*, 1203–1217.
- [4] Primiceri, E., Chiriaco, M. S., Rinaldi, R., Maruccio, G., *Lab Chip* 2013, *13*, 3789–3802.
- [5] Yan, S., Zhang, J., Yuan, D., Li, W., *Electrophoresis* 2017, *38*, 238–249.
- [6] Gao, Y., Li, W., Pappas, D., *Analyst* 2013, *138*, 4714–4721.
- [7] Salafi, T., Zeming, K. K., Zhang, Y., *Lab Chip* 2017, *17*, 11–33.
- [8] Antfolk, M., Laurell, T., *Anal. Chim. Acta* 2017, *965*, 9–35.
- [9] Dalili, A., Samiei, E., Hoorfar, M., *Analyst* 2019, *144*, 87–113.
- [10] Gong, Y., Fan, N., Yang, X., Peng, B., Jiang, H., *Electrophoresis* 2019, *40*, 1212–1229.
- [11] Lewpiriyawong, N., Yang, C., *Electrophoresis* 2014, *35*, 714–720.
- [12] Li, P., Mao, Z., Peng, L., Zhou, Y., Chen, P.-H., Huang, C. I., Truica, J. J., Drabick, S. W., El-Deiry, M., Dao, S., Suresh, S., Huang, T. J., *Proc. Natl. Acad. Sci. USA* 2015, *112*, 4970–4975.
- [13] Geislinger, T. M., Stamp, M. E. M., Wixforth, A., Franke, T., *Appl. Phys. Lett.* 2015, *107*, 203702.
- [14] Berendsen, J. T. W., Eijkel, J. C. T., Wetzels, A. M., Segerink, L. I., *Microsyst. Nanoeng.* 2019, *5*, 24.
- [15] Yamada, M., Seki, M., *Lab Chip* 2005, *5*, 1233–1239.

- [16] Sugaya, S., Yamada, M., Seki, M., *Biomicrofluidics* 2011, 5, 024103.
- [17] Jung, H., Chun, M.-S., Chang, M.-S., *Analyst* 2015, 140, 1265–1274.
- [18] Fouet, M., Mader, M.-A., Irain, S., Yanha, Z., Naillon, A., Cargou, S., Gué, A.-M., Joseph, P., *Lab Chip* 2016, 16, 720–733.
- [19] Di Carlo, D., Irimia, D., Tompkins, R. G., Toner, M., *Proc. Natl. Acad. Sci. USA* 2007, 104, 18892–18897.
- [20] Nakagawa, N., Yabu, T., Otomo, R., Kase, A., Makino, M., Itano, T., Sugihara-Seki, M., *J. Fluid Mech.* 2015, 779, 776–793.
- [21] Lu, X., Zhu, L., Hua, R., Xuan, X., *Appl. Phys. Lett.* 2015, 107, 264102.
- [22] Di Carlo, D., *Lab Chip* 2009, 9, 3038–3046.
- [23] Nivedita, N., Ligrani, P., Papautsky, I., *Sci. Rep.* 2017, 7, 44072.
- [24] Oh, K. W., Lee, K., Ahn, B., Furlani, E. P., *Lab Chip* 2012, 12, 515–545.
- [25] Zhao, C., Yang, C., *Adv. Colloid Interface Sci.* 2013, 201, 94–108.
- [26] Mehri, R., Mavriplis, C., Fenech, M., *PLoS One* 2018, 13, e0199911.
- [27] Yoon, K., Jung, H. W., Chun, M.-S., *Rheol. Acta* 2017, 56, 915–926.
- [28] Deen, W. M., *Analysis of Transport Phenomena*, Oxford University Press, New York 1998.
- [29] Ho, B. P., Leal, L. G., *J. Fluid Mech.* 1974, 65, 365–400.
- [30] Schonberg, J. A., Hinch, E. J., *J. Fluid Mech.* 1989, 203, 517–524.
- [31] Shivhare, P. K., Bhadra, A., Sajeesh, P., Prabhakar, A., Sen, A. K., *Microfluid. Nanofluid.* 2016, 20, 86.
- [32] Bruus, H., *Theoretical Microfluidics*, Oxford University Press, New York 2008.
- [33] Ceylan, K., Herdem, S., Abbasov, T., *Powder Technol.* 1999, 103, 286–291.
- [34] COMSOL Multiphysics Version 5.3a, *Users Guide*, COMSOL Inc., 2017.